Aerospace Science and Technology 129 (2022) 107826

Contents lists available at ScienceDirect

Aerospace Science and Technology

www.elsevier.com/locate/aescte

Aerodynamics of a short intake in crosswind

Luca Boscagli *, Robert Christie, David MacManus, Tommaso Piovesan

Propulsion Engineering Centre, School of Aerospace Transport and Manufacturing, Cranfield University, Bedfordshire, MK43 0AL, UK

ARTICLE INFO

Article history:
Received 8 April 2022
Received in revised form 31 July 2022
Accepted 16 August 2022
Available online 22 August 2022
Communicated by Mehdi Ghoreyshi

Keywords:
Short intake
CFD
Crosswind
Unsteady
Turbofan

ABSTRACT

The next generation of turbofan aero-engines are likely to have an increase in fan diameter to reduce the specific thrust and increase the overall propulsive efficiency. More compact nacelles with possibly shorter intakes may be used to reduce weight and drag and achieve a net reduction of fuel consumption. For these compact nacelles a key consideration is the design of the short intake at the off-design conditions such as crosswind and high incidence operations. The close coupled interaction between a short intake and the fan at these off-design conditions is one of the key challenges. Previous work focused on the impact of short intake aerodynamics on the fan but there is a similar requirement to understand the impact of the fan on the viable short intake design space. This paper addresses the influence of the fan on the separation onset of the flow within a short intake under crosswind conditions. The effect of the fan on the separation characteristics of the intake boundary layer was considered both from a steady and an unsteady point of view. A hierarchy of fan computational models was used to separately assess the different aerodynamic contributions and to evaluate a net effect of the fan on the intake critical condition. Steady computational fluid dynamics analyses showed a notable positive effect of the fan on total pressure loss at post-separation conditions relative to a configuration without the fan. However, unsteady analyses revealed that fan unsteadiness has an adverse impact on the intake separation characteristics which reduces the intake critical conditions by about 15%. The main mechanisms behind the unsteady interaction were identified. Overall this work addresses, for the first time, the role of fan unsteadiness on the separation characteristics of the boundary layer within a short intake in crosswind.

1. Introduction

The next generation of high efficiency turbofans will be characterised by larger fan diameters, which in turn could lead to an increase in nacelle weight and drag. These two negative aspects can be partially counteracted through the use of more compact nacelle, intake and exhaust systems [1–4]. The design of a short intake can be challenging because of the reduced internal diffusion capability and the non-negligible interaction of the flow between the intake and the fan. This can be important during take-off, climb-out and crosswind conditions where a distorted flow may be expected. Moreover, at these conditions the flow along the lip can locally be supersonic and Shockwave Boundary Layer Interactions (SBLI) may occur. Coschignano [5,6] conducted a 2D experimental study of SBLI under take-off conditions. The occurrence of a λ shock wave and separation onset were investigated as a function of the angle of attack, Reynolds number and lip shape. A notable sensitivity of the separation of the boundary layer to SBLI topology was demonstrated. Peters [7] provided an insight into a range of potential issues for short intake design at high incidence. The key finding was that the design of a viable short intake seems to be limited by a high Mach number region at the fan face which leads the rotor to operate close to choke. This resulted in an increase in distortion levels and a reduction in fan operability.

Several publications addressed the problem of fan-intake interaction at high incidence. Cao [8] provided an extensive numerical study, using full 3D unsteady CFD, on fan interaction with separated flow within an intake at high incidence. Depending on the ratio between the length of the intake (L_{in}) and the fan diameter (D_{fan}), the fan can either reduce the distortion levels after separation or delay the separation onset. Ma [9] assessed the influence of turbulence modelling for a prescribed fan model. Large Eddy Simulations (LES) and Reynolds-Averaged Navier-Stokes (RANS) simulations combined with a lower order model for the fan [10,11] were compared. The main conclusion was that the use of eddy resolving methods might only produce marginal differences on the prediction of total pressure distortions when applied in combination with lower order fan model. Carnevale [12] analysed a conventional civil aero-engine intake at high incidence conditions and both aspirated and powered configurations were considered by means of

* Corresponding author.
E-mail address: luca.boscagli@cranfield.ac.uk (L. Boscagli).

https://doi.org/10.1016/j.ast.2022.107826

Nomenclature

Acronyms

AIP	Aerodynamic Interface Plane
CFD	Computational Fluid Dynamics
CFL	Courant-Friedrichs-Lewy condition
EXP	Experiments
$IBMSG$	Immersed Boundary Method with Smeared Geometry
$RANS$	Reynolds Averaged Navier Stokes
$SBLI$	Shock-wave Boundary Layer Interaction
TRF	Time Resolved Fan
$URANS$	Unsteady Reynolds Averaged Navier Stokes

Greek letters

β	Relative axial whirl angle ..... [°]
β_{ma}	Blade metal angle ..... [°]
δ	Distance [m] or angle [°]
ω_{fan}	Fan rotational speed ..... [rad/s]
Φ	Flow coefficient [−]
ϕ	Azimuthal coordinate ..... [°]
ρ	Density ..... [kg/m^3]

Subscripts

∞	Freestream
bp	Blade passing
$diff$	Intake diffuser
hi	Intake highlight
in	Intake
$pitch$	Blade pitch
ref	Reference condition
$wall$	Intake surface

Variables

$\dot{m}_{fan}$	Mass flow at the fan face [kg/s]
$\overline{M_{abs}}$	Circumferentially averaged absolute Mach number [−]
$\overline{P_0}$	Area averaged total pressure [Pa]
τ_x	Axial wall shear stress ..... [Pa]
A	Area ..... [m^2]
D	Diameter ..... [m]
$DC60$	Total pressure distortion metric ..... [−]
f	Frequency ..... [Hz]
i	Blade incidence angle ..... [°]
IPR	Inlet Pressure Recovery ..... [−]
L	Length scale ..... [m]
M_{abs}	Absolute Mach number ..... [−]
$MFCR$	Mass Flow Capture Ratio ..... [−]
P_0, P	Total and static pressure ..... [Pa]
PR	Pressure Recovery ..... [−]
q	Dynamic head ..... [Pa]
R	Radius ..... [m]
r	Radial coordinate ..... [m]
$RTPR$	Rotor Total Pressure Ratio ..... [−]
t	Time scale ..... [s]
T_0, T	Total and static temperature ..... [K]
U, V	Velocity scale ..... [m/s]
U_{AIP}	Area averaged velocity at the AIP ..... [m/S]
V_x	Axial velocity ..... [m/s]
x	Axial coordinate ..... [m]
x^*	Non-dimensional axial coordinate ..... [−]

steady and unsteady RANS methods, respectively. A beneficial effect of the fan in terms of reduction in total pressure distortions was observed when the intake flow was separated. No significant differences were shown between the aspirated and powered configurations at lower distortion levels. The presence of the fan was able to improve the amplitude of the lower spatial harmonic components (engine-order, EO) of static pressure fluctuations upstream of the fan. The latter behaviour was observed for EO below 8 although the contribution of blade-passing EO for the powered configuration at critical or sub-critical condition was not analysed. For the aspirated case at sub-critical conditions the spectrum of static pressure fluctuations showed a clear signature at 1EO. The aspirated case was also assessed in crosswind conditions and the spectrum of static pressure fluctuations had a notable contribution at higher engine-orders such as 4 and 8. The latter behaviour was mainly attributed to the combined presence of a ground vortex and the total pressure distortions generated within the boundary layer on the windward side of the intake. Zhang [13] carried out a parametric study about the effect of inlet distortions on the prediction of fan stall and unsteady simulations were done with a numerical representation of inlet total pressure distortions. A larger loss in fan stall margin was observed with a reduction of fan rotational speed. Within the context of a complex intake and Boundary Layer Ingestion (BLI), Provenza [14] showed how the frequency content of inlet flow distortions can affect the fan at 1EO and limit the fan operability range. Also, the overall fan performance was affected by highly disturbed flow which developed along the intake. Gunn [15] performed experimental measurements of a low speed fan which operated with a prescribed total pressure loss within a 60° sector. It highlighted how inlet steady total pressure distortions can lead to a 5.3% reduction in fan stage total-to-total efficiency primarily due to an increase in rotor blade incidence angle relative to the fan design condition. Vadlamani [16] investigated fan intake interaction for a short intake at high incidence through unsteady time resolved fan computational analyses. Two different signatures were identified in the spectrum of the static pressure fluctuations. The higher frequency range was dominated by blade passing while the lower frequency one was associated to shock unsteadiness on the intake lip. The mechanism behind the unsteady SBLI though was not identified but a possible sub-harmonic interaction between blade passing and shock unsteadiness was postulated. Mohankumar [17] studied a short intake at high incidence and showed three main aerodynamic interaction mechanisms between the intake and the fan that should guide the fan design.

Aero-engine intakes under crosswind conditions were also the subject of extensive numerical and experimental investigations. The intake flow in crosswind is rather complex as it can exhibit lip separation as well as interaction with the ground which can lead to ground vortex formation. Murphy [18] provided a detailed experimental investigation of the influence of crosswind velocity, approaching boundary layer profile as well as ground clearance on the characteristic of the ground vortex and flow distortions within a cylindrical intake. Freeman and Rowe [19] performed an experimental investigation of a high by-pass ratio turbofan engine in ambient wind conditions with an artificial ground also installed to replicate the engine-inlet ground clearance. The intake flow exhibited an oscillatory behaviour from attached to separated that could drive the fan into stall. Hall and Hynes [20,21] experimentally investigated the interaction of an aero-engine intake with natural wind. A comparison between the steady and unsteady measurements showed that the statistics of intake flow separation and reattachment could be predicted through the steady measurements and the statistics of the natural wind. Colin [22] developed a CFD methodology to compute intake flow in crosswind and the main

challenges from a numerical modelling point of view were highlighted. In particular the notable differences in the flow regime within the intake compared to freestream produced a large disparity between convective modes and acoustic modes. A preconditioning technique was required to damp the acoustic mode at the start of the steady simulations and avoid divergence. The case study involved a long intake in crosswind with no ground plane and no fan. The flow within an intake in crosswind may experience severe acceleration on the lip that can induce relaminarization, separation and transition to turbulence [23]. Vadlamani [23] studied a quasi-2D intake in crosswind at a Reynolds number based on intake lip length and fan face velocity of about 10^4 and 10^5. The boundary layer was fully turbulent at those operating conditions and it was observed that relaminarization was unlikely to occur. Burnazzi [24] studied a short intake in crosswind with no ground and no fan. Steady RANS simulations were compared against eddy-resolving analysis and experimental data. Steady RANS over-predicted total pressure distortions relative to experiments and could not predict flow reattachment with severe adverse streamwise pressure gradient. Schnell [25] performed CFD analyses of a short intake ($L_{diff}/D_{fan} = 0.3$) in crosswind with a mixing-plane boundary condition for the fan and results were compared with an intake in headwind conditions. A notable drop in fan efficiency occurred in crosswind compared to the headwind condition. Minaker [26] performed steady RANS for a short intake in crosswind without the ground. Analyses included a full annulus for the fan that was modelled through a body force approach and two different fan stages were used. A range of crosswind velocity was studied and the prediction of the separation onset of the boundary layer within the intake was within 5% agreement for the two fan models. Steady RANS analyses were considered sufficient to understand the ability of the fan to capture fan-intake interaction. Lee [27] performed unsteady CFD analyses of an intake ($L_{in}/D_{fan} \approx 0.5$) in crosswind with fan interaction and no ground. The engine mass flow and crosswind velocity were such that a transonic flow developed on the intake lip. Notable reductions in fan stall margin were found when the intake exhibited lip separation. An increase in fan loading and fan rotational speed showed a positive effect on the suppression of intake total pressure distortion caused by lip flow separation. Crosswind with no lip separation were also analysed and it was shown that fan stall could still be initiated by an increase in blade incidence angle at the tip associated to the presence of the trailing vortices. Awes [28] studied the impact of ground vortex-like distortions on fan stall inception. A criterion based on critical fan blade incidence angle was developed and the importance of vortex distortions on fan rotating stall was shown.

1.1. Scope of the present work

The coupled interaction between fan and short intake at high incidence was widely discussed in the literature. A primary impact of the fan on the reduction of total pressure distortions and delay of the separation onset of the boundary layer within the intake was generally agreed. The interaction mechanisms relative to the time average flow field were identified and primarily attributed to a radial mass flow redistribution of the intake flow at the nominal fan face. Considerable effort was spent in recent years to develop lower order fan models such that fan-intake coupled interaction could be modelled within the intake design process [7,10]. The unsteady interaction between the fan and the intake has generally received less attention and the problem was mainly assessed from a fan design point of view and either attached or separated intake flow conditions were analysed. Considerations were mostly made on the effect of the fan on the reduction of total pressure distortion at intake post-separation condition and fan stall delay. Intake design requires a good knowledge of separation onset which is usually referred to a critical condition. Changes in operating conditions can have a notable impact on the intake critical condition. The relative bulk effect of the fan on the intake flow at post-critical condition was established at high-incidence and in crosswind without a ground. However, the spatial and temporal contributions of the fan on the flow within a short intake at critical and sub-critical condition were never quantitatively and qualitatively assessed. In particular, the influence of fan unsteadiness on the separation onset of the boundary layer within a short intake is not established yet. This work addresses the impact of the fan on the flow field within a short intake in crosswind conditions with the presence of the ground. A hierarchy of fan computational models is exploited to decouple the different aerodynamic mechanisms and to establish the net impact of the fan on the critical condition of a short intake in crosswind.

2. Computational methods

2.1. CFD Solver

An unstructured finite volume solver was used within this work (HYDRA, [29]). An approximate Riemann solver of Roe is used for computation of the numerical fluxes based on a second-order MUSCL scheme for the spatial discretization [30]. To prevent numerical dispersion around discontinuities in the flow (e.g. shockwaves) a pseudo-laplacians approach [31] is used to blend between first and second order. The evaluation of the gradients is done through a Green-Gauss method [31]. An implicit second order backward difference scheme is used for the time advancement [32]. Reynolds Averaged Navier Stokes (RANS) equations are solved within this work. Spalart-Allmaras (SA) was used as the turbulence model with a turbulent production term based on vorticity and strain [33]. The choice of the turbulence model was based on previous work on the literature for intake under off-design conditions with lower order fan models [8,16,12]. A low Mach number preconditioning technique was also enabled to damp the acoustic modes and improve the initial convergence. For multi-stage single passage turbomachinery computations a steady Mixing-Plane (MP) boundary condition [34] was used at the interface between rotor and stator parts which operate into different relative reference of frame. For steady and unsteady full-annulus computations a sliding plane boundary condition was used. At the interface where a sliding plane is applied the adjacent sub-domains are extruded in the direction normal to the interface and a one cell row overlap will form [32]. Thus, the sliding plane has both an internal and an external (extruded) boundary for each sub-domain. The primitive variables at the nodes in the exterior surface in each sub-domain are obtained from the interpolation of the values on the interior surface of the adjacent sub-domain. A sliding plane boundary condition was used for fan-intake coupled analyses and it was complemented with unsteady RANS to capture both the change in relative reference of frame and the correct temporal evolution of the position of the blade row. A lower order fan model was also used and referred as Immersed Boundary Method for Smeared Geometries (IBMSG, [10]). The model assumes that an infinite number of 'zero-thickness' blades can model a rotating fan. The forces parallel and normal to the blade camber line are circumferentially averaged within every cell in the region bounded by the blades. The IBMSG model used in the present work was previously applied to the analysis of an intake flow at high incidence for both attached and separated cases [8].

2.2. CFD method verification and validation

A baseline case study, using an unpowered intake, was considered to demonstrate the CFD solver capabilities to deal with highly

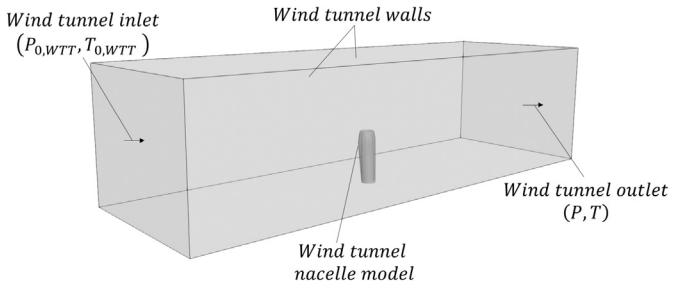

Fig. 1. Schematic of the wind tunnel domain for the validation studies under crosswind conditions.

Table 1
Average grid resolution within the intake.

Mesh level	Number of nodes [$\times 10^6$]	$\Delta x/r_{fan}$[%]	$\Delta r/r_{fan}$[%]	$\Delta\phi$[°]	y^+
1	6.8	1.7	0.7	2.5	1
2	10.8	1.5	0.65	1.8	1
3	35.2	1.15	0.5	0.8	1

distorted flow and separation due to strong adverse streamwise pressure gradient and shock-wave boundary layer interaction. The CFD solver turbomachinery capabilities were validated through single stage turbomachinery analyses.

2.2.1. Intake in crosswind

Baseline validation analyses were done for a non-axisymmetric intake geometry with no ground plane and no fan in a wind tunnel configuration (Fig. 1). Under the wind tunnel conditions the intake Reynolds number ($Re_{D_{hi}}$) was 1.3×10^6. The intake Mass Flow Capture Ratio ($MFCR$ [35], Eq. (1)) is defined as the ratio between the far upstream area of the ingested streamtube (A_∞) and the intake highlight area (A_{hi}). The MFCR was controlled through the intake mass flow ($\dot{m}_{fan}$) with the wind tunnel crossflow (U_∞) held constant. The MFCR was referred to a reference attached condition ($MFCR_{ref}$) and redefined as $MFCR^* = MFCR - MFCR_{ref}$. Total pressure distortion and loss were quantified at the Aerodynamic Interface Plane (AIP) based on DC60 (Eq. (2)) and IPR (Eq. (3)) respectively.

$$MFCR = \frac{A_\infty}{A_{hi}} = \frac{\dot{m}_{fan}}{\rho_\infty U_\infty A_{hi}} \tag{1}$$

$$DC60 = \frac{\overline{P_{0,60}} - \overline{P_{0,AIP}}}{\overline{q_{AIP}}} \tag{2}$$

$$IPR = \frac{\overline{P_{0,AIP}}}{P_{0,WTT}} \tag{3}$$

In Eq. (2) $\overline{P_{0,60}}$ is the lowest area-averaged total pressure in a 60° sector at the AIP, $\overline{P_{0,AIP}}$ and $\overline{q_{AIP}}$ are the area-averaged total pressure and dynamic head, respectively. In Eq. (3) $P_{0,WTT}$ is the wind tunnel inlet total pressure. The experimental uncertainty on MFCR ($\pm 0.014 MFCR$) was estimated based on the experimental uncertainty on mass flow and wind tunnel inlet velocity. A grid independence study was carried out using the recommended approach by Celik [36]. Three different levels of grid refinement were investigated which encompassed 6.8×10^6, 10.8×10^6, 35.2×10^6 nodes (Table 1). The grids are referred to as level 1, 2 and 3. The Grid Convergence Index (GCI) was computed at attached flow conditions ($MFCR^* = 0$) and the influence of the spatial discretization on the separation onset was also quantified. Level 2 grid was sufficiently grid independent with a GCI compared to level 3 grid of 0.014% and 5.6% when applied to IPR and DC60 respectively. A discretization error was also quantified based on the isentropic Mach

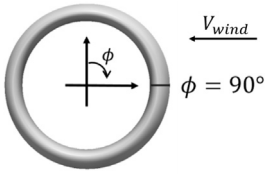

Fig. 2. Intake azimuthal coordinate definition and wind direction.

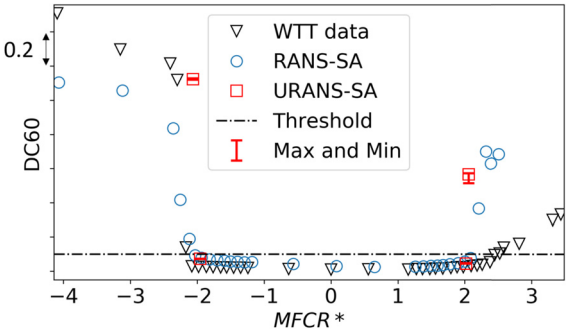

Fig. 3. DC60 distribution against $MFCR^*$. $Re_{D_{hi}} = 1.3\times10^6$. Steady and unsteady RANS results comparison against Wind Tunnel Test (WTT) data.

(M_{ise}, Eq. (4)) evaluated on the intake surface. The GCI was computed based on the peak M_{ise} on the windward side of the intake, at an azimuthal position (ϕ) 90° from the top dead centre (Fig. 2). Level 2 grid had a GCI compared to level 3 grid of 0.67%.

$$M_{ise} = \sqrt{\frac{2}{\gamma-1}\left[\left(\frac{P_{0,\infty}}{P}\right)^{\frac{\gamma-1}{\gamma}} - 1\right]} \tag{4}$$

DC60 provides a measure of the level of flow distortions at the AIP. The operating conditions where DC60 is just below the threshold are of main interest from the intake design point of view and are referred to critical conditions. For an intake in crosswind two regions where the total pressure distortions exceed the threshold are identifiable (Fig. 3) and both of them are typically experienced by the intake as the mass flow through the engine is increased. The two regions are characterised by two different flow regimes and flow topology and the separation characteristics of the intake boundary layer are also different. On the lower end of the DC60 distribution ($-2 < MFCR^* < -4$, Fig. 3) the flow within the intake is subsonic and it has high levels of diffusion with an open boundary layer separation that starts from the intake highlight. At this flow regime the separation of the intake boundary layer is typically characterised by hysteresis [21] which from a computational point of view is difficult to model [22]. On the upper end of the DC60 curve ($MFCR^* > 2$, Fig. 3), the flow on the intake lip is transonic and as the engine mass flow is increased a shock induced separation may occur with a consequent increase in total pressure loss and distortions. In this work the separation characteristics of the boundary layer within a short intake with fan interaction were analysed at the transonic flow regime.

The influence of spatial discretization on critical MFCR was quantified using grid level 1, 2 and 3. Relative to the experimental critical MFCR ($MFCR_{c,WTT}$), at the transonic regime ($MFCR^* > 2$) the influence of spatial discretization on the prediction of $MFCR_c$ was about $0.015 MFCR_{c,WTT}$. Thus, grid level 2 was sufficiently grid independent and it was used to quantify the prediction of $MFCR_c$ relative to experimental data (Eq. (5)). The steady RANS with SA as the turbulence model were able to predict $MFCR_c$ with $\Delta MFCR_c \approx 6\%$ accuracy (Fig. 3) at transonic ($MFCR^* > 2$) regime.

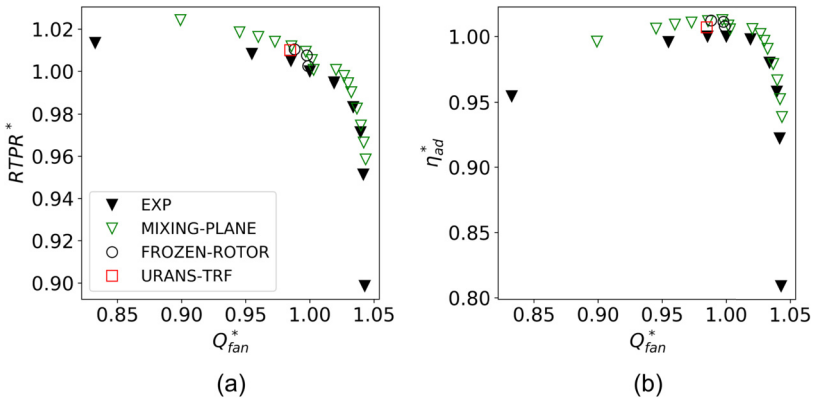

Fig. 4. Distribution of normalized (a) rotor total pressure ratio ($RTPR^*$) and (b) rotor adiabatic efficiency (η^*_{ad}) against normalized fan capacity (Q^*_{fan}). Steady RANS Mixing-Plane and Frozen-Rotor (FR) and URANS Time Resolved Fan (TRF) comparison against rig data (EXP).

$$\Delta MFCR_c[\%] = \frac{MFCR_{c,CFD} - MFCR_{c,WTT}}{MFCR_{c,WTT}} 100 \tag{5}$$

The critical MFCR was also evaluated through unsteady RANS (Fig. 3). A convective time (t_c) defined as the ratio between the intake length (L_{in}) and the average flow velocity at the AIP ($\overline{U}_{AIP}$) was used to normalize the computational time-step (dt_{CFD}). A computational time-step assessment was done with $dt_{CFD} = t_c/5$, $t_c/10$ and $t_c/20$. $dt_{CFD} = t_c/10$ was used as the simulations were sufficiently time-step independent. The unsteady RANS were initialised with steady RANS at the corresponding operating condition and after an initial transient of about $40t_c$ the simulations were advanced in time for a further $60t_c$ that were included in the analyses. Overall the unsteady RANS agreed with the steady prediction of critical MFCR with a discrepancy relative to the RANS results of about ±1-2% which is below the discretization error. Thus, from the intake design point of view steady RANS are adequate to predict the intake critical conditions for an aspirated intake.

2.2.2. Isolated fan stage

The CFD solver turbomachinery capabilities were validated through single stage turbomachinery computations. The test configuration comprised a fan, Outlet Guide Vane (OGV) and Engine Section Stator (ESS). The comparison between CFD and experiments was done based on Rotor Total Pressure Ratio ($RTPR = \frac{P_{0,fan-outlet}}{P_{0,fan-face}}$) and rotor adiabatic efficiency (η_{ad}). Fan capacity (Q_{fan}), $RTPR$ and η_{ad} were normalized with the experimental values at fan peak efficiency point and referred as Q^*_{fan}, $RPTR^*$ and η^*_{ad} respectively. Single passage steady RANS with mixing-plane boundary conditions were done to assess grid sensitivity [36]. Three different levels of grid refinement were generated whose overall size was 4.4×10^6, 8.2×10^6 and 16.2×10^6 nodes. The grids are referred to as level 1, 2 and 3 respectively. The mass flow at the ESS outlet was fixed in agreement with test rig approach and static pressure at the OGV outlet was varied to move across the fan characteristic. The purpose of this work is the analysis of intake performance and therefore level 1 grid was considered sufficiently grid independent with a GCI with respect to level 2 grid of 0.04% and 0.035% when applied to RTPR and η_{ad} respectively. Full annulus grids were then generated for fan, OGV and ESS and further CFD analyses were done at fan peak efficiency point. Both steady RANS with Frozen-Rotor (FR) and URANS with sliding plane boundary conditions were done (Fig. 4). For the full-annulus unsteady analyses 60 time-steps per blade-passing time (t_{bp}) were selected [12] and the simulation encompassed 3 fan revolutions after an initial transient of about 3 more fan revolutions. The agreement between experiments and CFD was quantified as follows,

$$\Delta RTPR^* = RTPR^*_{CFD} - RTPR^*_{EXP}, \quad \Delta\eta^*_{ad} = \eta^*_{ad,CFD} - \eta^*_{ad,EXP} \tag{6}$$

Across the different CFD models $\Delta RTPR^*$ and $\Delta\eta^*_{ad}$ were below 0.01 and 1.2% respectively (Fig. 4). Overall the computational approach was considered acceptable within the context of this work which is focused on the analysis of the separation characteristics of the boundary layer within a short intake with fan interaction.

2.3. Short intake under crosswind conditions

2.3.1. Computational domain and boundary conditions

A range of steady and unsteady CFD analyses was assessed for a short intake in crosswind with $L_{in}/D_{fan} = 0.35$. The computational domain for the short intake simulations encompassed a quarter of a sphere which incorporates intake, ground plane and fan. The edges of the computational domain were positioned about $35D_{fan}$ away from the intake which is far enough based on previous work [16,27]. Static pressure far-field boundary conditions were applied at the freestream based on the wind velocity and total pressure (P_0) and total temperature (T_0) at sea-level static. The crosswind velocity direction was such that the inlet vortex and the fan were counter-rotating. Ground plane, intake, spinner and fan cowl were modelled as viscous walls. A hierarchy of numerical fan models was explored (Fig. 5) and three different computational domains were generated and spatially discretized through a fully structured approach [37]. The steady and unsteady RANS-IBMSG encompassed one single domain and the presence of the fan was accounted for with an overall grid size of about 14 million nodes. The unsteady Time Resolved Fan (TRF) case included the complete fan assembly and one single blade passage for the Outlet Guide Vane (OGV) and one for the Engine Section Stator (ESS). The turbomachinery components were meshed through a fully structured approach [38] where a typical rig tip clearance was included in the fan model and radially discretized with 35 nodes. The intake geometry for the TRF analyses was meshed up to the interface with the fan face to then accommodate the turbomachinery domain. A sliding plane boundary condition [32] was applied at the interface between the intake and the fan. Circumferentially averaged (Mixing-Plane, MP) boundary conditions where applied at the interfaces between fan, OGV and ESS. A case without the fan was also considered and referred as aspirated. A simplified annular duct was added after the nominal fan face to further extend the intake computational domain. For all three CFD models a $y^+ \approx 1$ near-wall resolution was ensured and the engine mass flow was controlled through a mass flow outlet boundary condition in agreement with previous work [16].

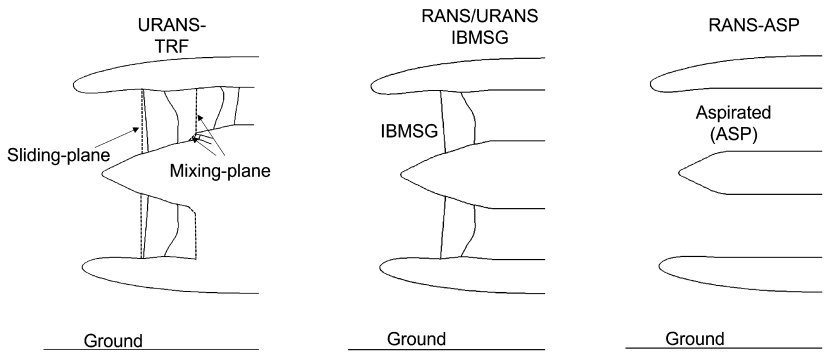

Fig. 5. CFD fan modelling hierarchy.

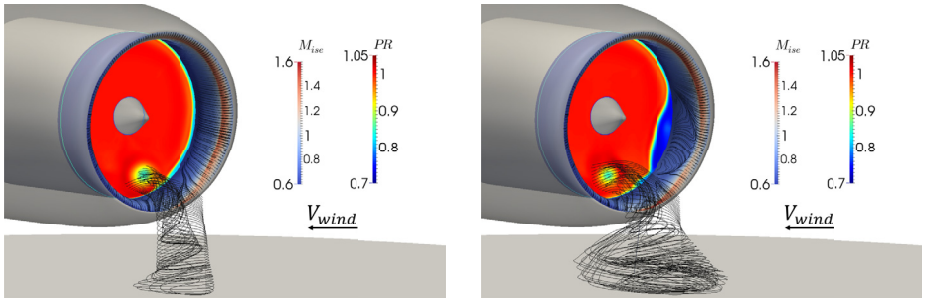

Fig. 6. (a) Critical ($V_{wind} = 28kts$) and (b) post-critical ($V_{wind} = 30kts$) conditions for the aspirated intake configuration (RANS-ASP).

The intake operated at sea-level static conditions with fixed engine mass flow to achieve the desired Mach number at the fan face. The wind velocity (V_{wind}) was then ranged between $V_{wind} =$ 20 to $30kts$ and $MFCR$ and $Re_{D_{hi}}$ varied accordingly between 13 and 7.8 and 0.7×10^6 and 1×10^6 respectively. A hierarchy of computational fan models was investigated (Fig. 5) and for the powered cases the fan operated with a transonic interaction at the blade tip. The comparison between the different CFD models was initially carried out based on IPR and percentage of reverse mass flow (Eq. (7)) at an AIP positioned $5\%R_{fan}$ upstream of the blade tip leading edge.

$$\dot{m}^-[\%] = \frac{\dot{m}^-}{\dot{m}_{AIP}} 100 \tag{7}$$

DC60 and other conventional total pressure distortion metrics can exhibit a non monotonic behaviour for such complex vortical flows and therefore they are not suitable to describe the overall status of the flow characteristics within an intake under crosswind conditions with ground interaction [39,40].

2.3.2. Unsteady analyses

The unsteady analyses were all initialised with a steady RANS solution at the corresponding operating conditions. The URANS-TRF were initialised with steady RANS with a frozen rotor interface and 60 time-steps per blade-passing time were selected for the temporal resolution [12,16] The ratio between the computational time-step (dt_{CFD}) and the global Courant-Friedrichs-Lewy (CFL) condition was $dt_{CFD}/CFL \approx 5.5 \times 10^{-6}$. The URANS-IBMSG were initialised with steady RANS-IBMSG and a computational time-step assessment was done at $V_{wind} = 30kts$. IPR time history was monitored and IPR temporal autocorrelation was evaluated once the initial transient was removed. The choice of dt_{CFD} did not largely affect the main flow 'time-scale' at the AIP but it had a notable impact on the predicted range of total pressure loss. Thus, $dt_{CFD} = t_{bp}/60$ was selected to ensure a fair comparison between URANS-IBMSG and URANS-TRF. After the initial transient effects, the unsteady analyses were advanced in time from 3 to 9 fan revolutions that were included in the analysis.

3. Results and discussion

Steady RANS simulations of an unpowered, or aspirated, intake (RANS-ASP) were initially done to establish the overall intake aerodynamic performance based on the greatest wind velocity that the intake was able to sustain without any flow separation at the AIP. The latter condition is referred to as critical crosswind velocity throughout the section and it determines the nominal design limits of the intake. At this maximum crosswind condition the intake flow around $\phi = 90°$ was locally supersonic and the ground vortex ingested within the intake generated a localised total pressure loss on the lower half of the intake (Fig. 6). The boundary layer within the intake at the AIP was attached at $V_{wind} = 28kts$ (Fig. 8) but then separated on the windward side ($\phi = 90°$) at $V_{wind} = 30kts$.

The isentropic Mach number (M_{ise}) distribution on the windward side of the intake ($\phi = 90°$) had a monotonic increase in the pre-shock M_{ise} from $V_{wind} = 20kts$ to $28kts$ and the shock axial position was almost unchanged (Fig. 7). When the crosswind velocity was further increased from $V_{wind} = 28kts$ to $30kts$ a shock induced separation on the intake lip extended to the AIP with a consequent large total pressure loss and highly non uniform flow at the AIP (Fig. 6b). The static pressure on the diffuser decreased and the shock moved towards the intake highlight with a pre-shock M_{ise} at the intake sideline ($\phi = 90°$) of about $M_{ise} = 1.5$ at critical ($V_{wind} = 28kts$) condition that reduced to about $M_{ise} = 1.35$ at post-critical ($V_{wind} = 30kts$) condition (Fig. 7).

For the powered intake configuration the fan is typically modelled using a low order fan model within the intake design process [7]. However, a hierarchical framework is needed to account for both steady and unsteady mechanisms and to evaluate the net effect of the fan on the separation characteristics of the intake boundary layer. In this section changes in the steady flow field due

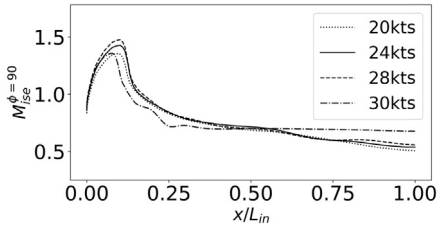

Fig. 7. Isentropic Mach number distribution on the intake surface at $\phi = 90°$ for the aspirated intake configuration (RANS-ASP).

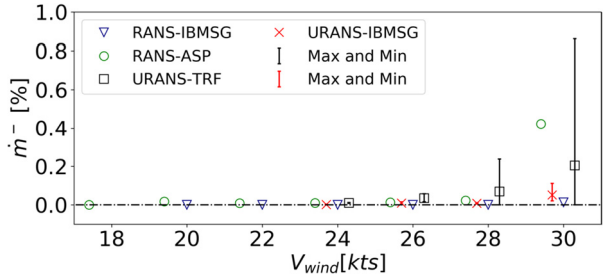

Fig. 8. Effect of crosswind velocity (V_{wind}) on reverse mass flow percentage ($\dot{m}^-$) at the AIP; x-offset added for more clarity.

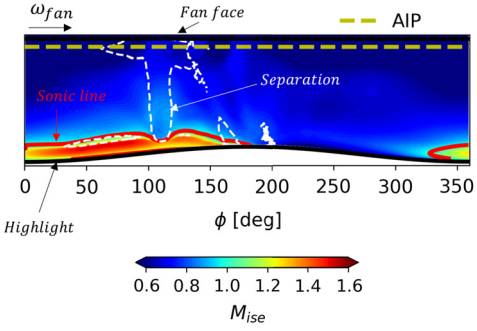

Fig. 9. Isentropic Mach number distribution and boundary layer separation on the unwrapped intake surface for the powered configuration (RANS-IBMSG) at $V_{wind} = 30kts$. Solid red line: $M_{ise} = 1$. Dashed white line: axial wall shear stress $\tau_x = 0$.

to the presence of the fan relative to an aspirated configuration are quantified using steady RANS computations and the lower order fan model (IBMSG, [10]) (Fig. 8). The unsteady interaction mechanisms are addressed in the subsequent sections (3.1 and 3.2) as they also play a major role on the prediction of the separation onset and characteristics of the intake boundary layer (Fig. 8).

At $V_{wind} = 28kts$ the boundary layer at the AIP in the powered (RANS-IBMSG) configuration was effectively attached with $\dot{m}^- < 0.001\%$ (Fig. 8). At $V_{wind} = 30kts$ for the powered (RANS-IBMSG) configuration there was a shock induced separation in the lower quadrant (Fig. 9) but the total pressure loss at the AIP were considerably reduced compared to the aspirated (RANS-ASP) configuration (Fig. 10). The fan radially redistributed the flow at the AIP (Fig. 11) and contributed to a more full, higher momentum boundary layer profile within the diffuser section on the windward side of the intake (Fig. 12b).

Previous experimental evidence [41] at take-off conditions showed that a lower momentum boundary layer profile in the post-shock region may produce a reduction in the effective camber of the intake lip. Thus, the shock location may shift towards the highlight with a likely more adverse interaction of the boundary layer with the pressure gradient within the diffuser. At the critical condition ($V_{wind} = 28kts$) the powered (RANS-IBMSG) and aspirated (RANS-ASP) configurations agreed both in terms of shock location and pre-shock M_{ise} at $\phi = 90°$ (Fig. 12a). However, at $V_{wind} = 30kts$ the radial extent of the separation in the diffuser section for the aspirated case was notably larger than for the powered (RANS-IBMSG) configuration, hence the notable differences in the isentropic Mach distribution at $\phi = 90°$ (Fig. 12a). Thus, the steady contribution of the fan at post-critical condition ($V_{wind} = 30kts$) reduced the extent of the separation of the intake boundary layer compared to the aspirated configuration and consequently it led to a beneficial reduction of the total pressure at the AIP which confirmed previous findings for a $L_{in}/D_{fan} = 0.5$ intake [27].

3.1. Impact of intake flow unsteadiness

Aero-engine intakes in crosswind are likely to exhibit high levels of flow unsteadiness even at critical or sub-critical conditions due to the presence of the ground vortex [42]. For a fixed intake ground clearance the levels of ground vortex unsteadiness tend to increase with crosswind velocity. Moreover, there was a closed, shock induced, separation at $V_{wind} = 28kts$ for the RANS-IBMSG which may also result in an unsteady shock-wave boundary layer interaction. Thus, from the intake design point of view it is important to evaluate the impact of intake flow unsteadiness on the intake critical conditions and to assess whether the temporal variation of the flow at the AIP affects the overall intake performance.

Compared with the steady RANS-IBMSG model, the URANS-IBMSG simulations provide an evaluation of the impact of intake flow unsteadiness on the prediction of the intake critical conditions. At $V_{wind} = 28kts$, compared with the steady model (RANS-IBMSG) the effect of the intake unsteadiness (URANS-IBMSG) on the separation characteristics was very small where $\dot{m}^-$ increased by 0% to 0.01% (Fig. 8). The steady RANS-IBMSG prediction of AIP total pressure distribution was in agreement with the time averaged URANS-IBMSG at the AIP at the same operating conditions (Fig. 10 at $V_{wind} = 28kts$). On the windward side of the intake ($\phi = 90°$) the maximum difference in peak isentropic Mach between RANS and URANS-IBMSG was relatively small at 0.01 (Fig. 13a). At the intake bottom dead centre ($\phi = 180$) the steady RANS-IBMSG underpredicted the peak M_{ise} by about 0.15 (Fig. 13b) compared to URANS-IBMSG. However, weak shock waves with a pre-shock Mach of about $M_{ise} = 1.1$ were predicted by the URANS-IBMSG. Thus, at $V_{wind} = 28kts$ the difference in the M_{ise} distribution between the steady and unsteady IBMSG computations was not primarily attributed to the presence of intake flow unsteadiness but to the inherent unsteady nature of the three dimensional flow field in crosswind.

At $V_{wind} = 30kts$ the URANS-IBMSG model showed unsteady shock-induced separation with fluctuations of about ± 0.08 in the pre-shock M_{ise} on the lower quadrant of the windward side of the intake (Fig. 8 and 14) and therefore a steady computation was inadequate. Steady RANS-IBMSG substantially underpredicted the amount of reverse mass flow at the AIP relative to the URANS-IBMSG and the total pressure distribution at the AIP also differed from both the instantaneous and time-average distribution predicted by URANS-IBMSG (Fig. 10). Overall, although there are differences in the post-critical regime where the intake flow unsteadiness is significant, there was good agreement between the unsteady (URANS-IBMSG) and steady (RANS-IBMGS) results in terms of the onset of the critical condition ($V_{wind} = 28kts$) from an intake design perspective.

3.1.1. Evaluation of the unsteady mechanisms

For the unsteady simulations with the low order fan IBMSG model (URANS-IMBSG), the source of the intake flow unsteadiness at $V_{wind} = 30kts$ was characterized through a frequency analysis [43] of the intake flow. Compared to blade passing frequency (f_{bp}),

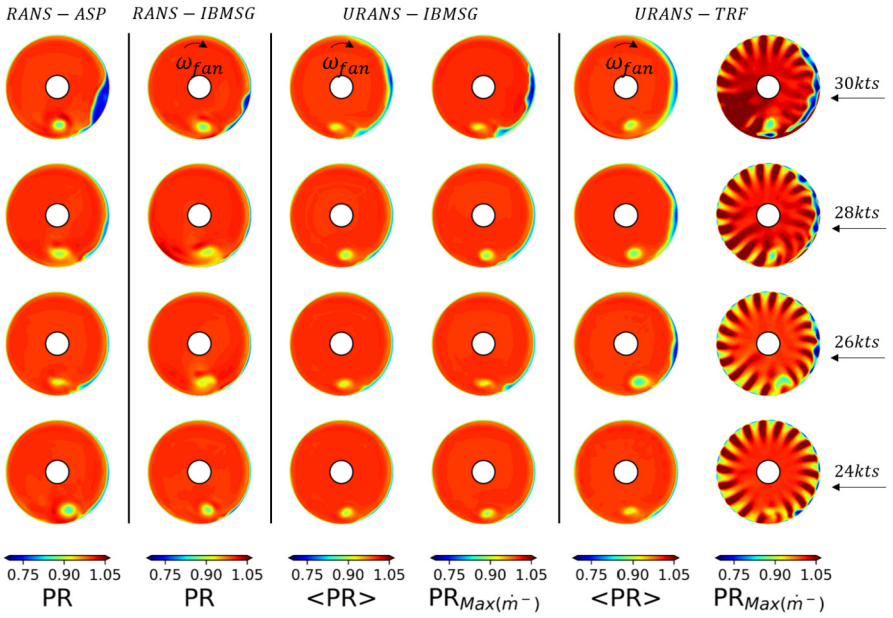

Fig. 10. Effect of crosswind velocity on total Pressure Recovery (PR) at AIP. Comparison between steady RANS-ASP and RANS-IBMSG and unsteady URANS-IBMSG and URANS-TRF. For the URANS-IBMSG and URANS-TRF both time average solutions ($\langle PR \rangle$) and instantaneous solution at maximum reversed mass flow ($\dot{m}^-$) are included.

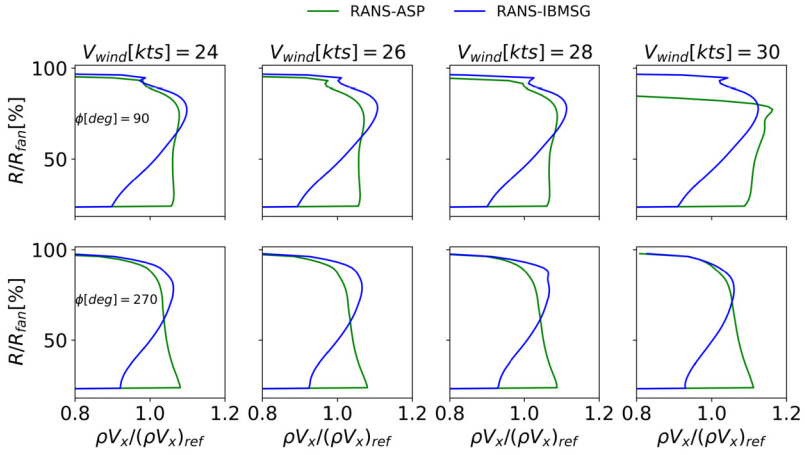

Fig. 11. Radial mass flux distribution at the AIP at $\phi = 90°$ and $\phi = 270°$ for the aspirated and powered (IBMSG) configurations.

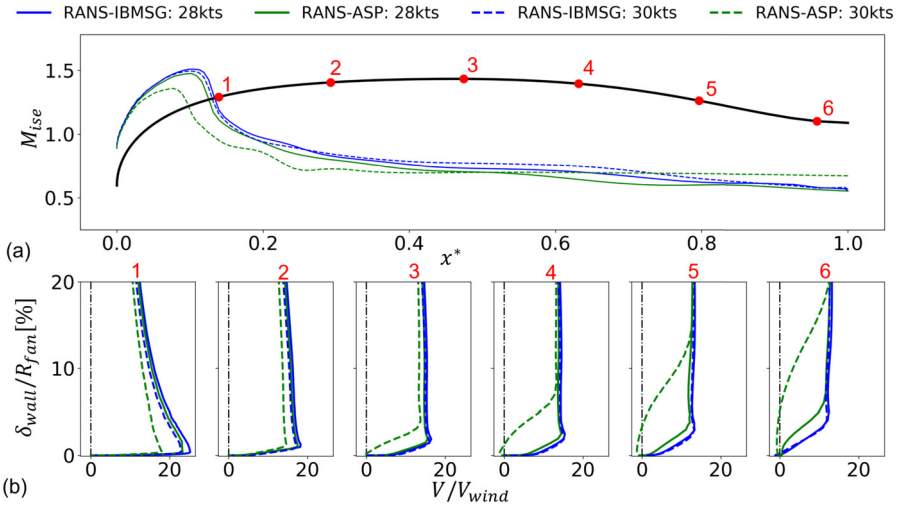

Fig. 12. (a) Isentropic Mach number profiles and (b) streamwise velocity profiles for the aspirated and powered (IBMSG) configurations at $\phi = 90°$.

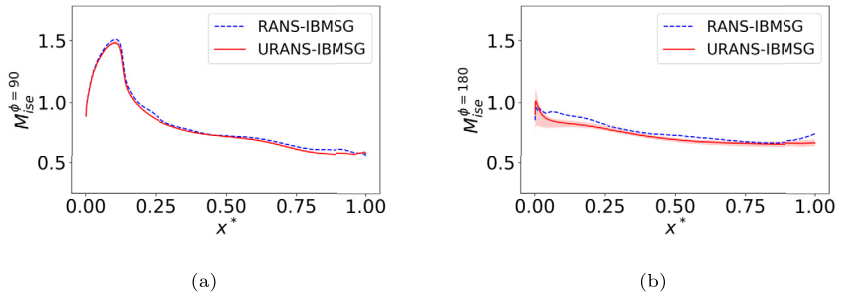

Fig. 13. Isentropic Mach number profiles at (a) $\phi = 90°$ and (b) 180° for the steady and unsteady powered (IBMSG) configuration at $V_{wind} = 28kts$. The shaded region refers to URANS-IBMSG and marks the max and minimum values through-out the fan revolutions.

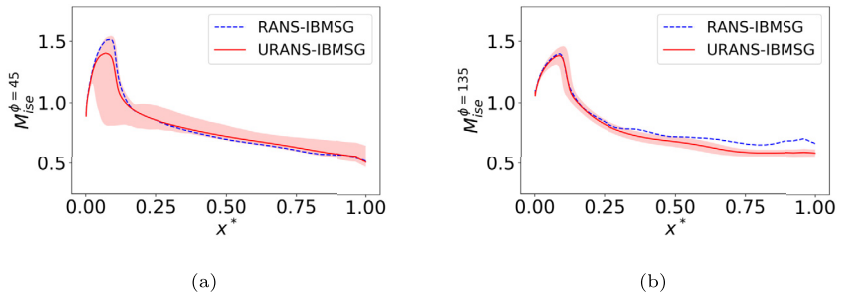

Fig. 14. Isentropic Mach number profiles at (a) $\phi = 45°$ and (b) 135° for the steady and unsteady powered (IBMSG) configurations at $V_{wind} = 30kts$. The shaded region refers to URANS-IBMSG and marks the max and minimum values through-out the fan revolutions.

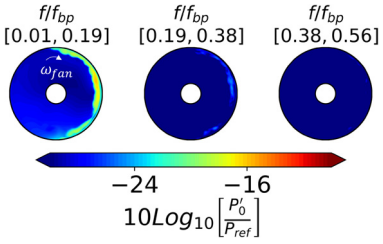

Fig. 15. Banded Fourier spectra of total pressure fluctuations at the AIP for the unsteady powered (IBMSG) configuration at $V_{wind} = 30kts$.

it is expected that the intake flow unsteadiness occurs at a relatively low frequency ($\left[f_{bp}/50,\ f_{bp}/10\right]$, [19,12,16]). To enable these two unsteady signatures to be distinguished the Fourier spectrum was subdivided into frequency bands with a frequency resolution $\Delta f \approx f_{bp}/5$. Banded Fourier spectra of the total pressure fluctuations at the AIP showed a clear spectral signature within the range $f/f_{bp} = [0.01, 0.19]$ (Fig. 15). The amplitude of the total pressure fluctuations (P_0') was normalised with a reference static pressure that corresponded to an ideal value of the static pressure at the nominal fan face (P_{ref}) if an isentropic process within the intake were assumed. The amplitude of the fluctuations was greater around the sideline of the intake ($\phi = 90°$) where a shock induced separation was previously observed and on the lower quadrant where the ground vortex was ingested. Thus, at $V_{wind} = 30kts$ it is argued that the spectral signature observed in the total pressure fluctuations at the AIP (Fig. 15) is mainly associated with unsteady separation due to the shock pulsation on the intake lip (Fig. 14).

The main characteristics of the ground vortex at the AIP plane were identified based on the vorticity disk method [44] and there was a low frequency oscillation of the radius of the core of the ground vortex (r_c). Scaled with the mean velocity at the AIP and fan diameter, the low frequency corresponded to a Strouhal (St) number of about $St = 0.09$. This is slightly greater compared to previous experimental observations in the literature for ground vortex [42] which report St in the range of $St = 0.01$ to 0.03. However, the amplitude of r_c fluctuations (Δr_c) was small relative to the fan radius (R_{fan}) with $\Delta r_c/R_{fan}$ below 1%. At $V_{wind} = 28kts$ no unsteady SBLI on the intake lip occurred within the same intake sector ($\phi = [45, 135]°$, Fig. 14) and therefore the differences between the RANS and URANS-IBMSG computations at $V_{wind} = 28kts$ were mainly associated to the ground vortex unsteadiness.

3.2. Impact of fan unsteadiness

As described in the previous section, the comparison between RANS and URANS IBMSG provide an evaluation of the effect of intake flow unsteadiness on the critical operating conditions for the intake. The Unsteady Time Resolved Fan (URANS-TRF) simulations then provide an additional evaluation of the coupled interaction of the unsteady fluctuations from the fan on the unsteady intake flow. Overall, when considered within the hierarchy of modelled configurations the critical intake operating point is affected by a range of flow field mechanisms. The total pressure loss at the AIP substantially reduces at the post-critical conditions ($V_{wind} = 30kts$) when the bulk, average effect of the fan is taken into account (RANS-ASP to RANS-IBMSG). This is predominately due to the radial mass flow redistribution which benefits the intake boundary layer characteristics. The effect of the intake unsteadiness alone (RANS-IBMSG to URANS-IBMSG) does not affect the critical crosswind velocity (V_{crit}). However it does affect the prediction of $\dot{m}^-$ and changes in the M_{ise} at the bottom dead center ($\phi = 180°$) are mainly associated with the ground vortex unsteadiness. Finally, the unsteady effects from the fan (URANS-IBMSG to URANS-TRF) adversely affect V_{crit}. Compared with the lower fidelity models (RANS-IMBSG, URANS IBMSG), the V_{crit} is reduced from $V_{wind} = 28kts$ to $24kts$ (Fig. 8).

For the URANS-TRF at $V_{wind} = 28kts$ there was unsteady separation of the boundary layer at the AIP (Fig. 8) and therefore a difference in terms of intake critical condition prediction was identified relative to RANS and URANS IBMSG. Both instantaneous and time average total pressure distribution at the AIP at $V_{wind} = 28kts$ were notably different for the URANS-IBMSG and URANS-TRF (Fig. 10). There was an unsteady shock wave boundary layer interaction at $V_{wind} = 28kts$ for the URANS-TRF and the peak isentropic

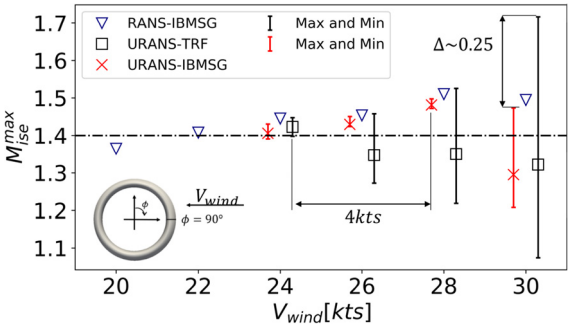

Fig. 16. Effect of crosswind speed on peak isentropic Mach number (M_{ise}^{max}) at $\phi = 90°$; x-offset added for more clarity.

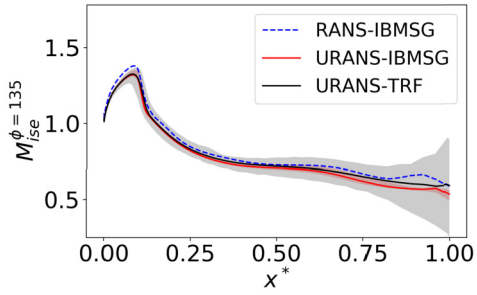

Fig. 17. Isentropic Mach number profiles at $\phi = 135°$ for RANS-IBMSG, URANS-IBMSG and URANS-TRF at $V_{wind} = 24kts$. For URANS cases the solid line is the time average solution, the shaded region marks the max and minimum values.

Mach at the intake sideline ($\phi = 90°$) showed fluctuations of about ± 0.2 around the time averaged value (Fig. 16). The total pressure losses at the AIP for the URANS-TRF were mainly associated with lip separation on the windward side of the intake. At $V_{wind} = 26kts$ the fluctuations on the peak isentropic Mach at $\phi = 90°$ for the URANS-TRF reduced to about ± 0.1 (Fig. 16) but the amplitude of the fluctuations was still notably greater than the ± 0.02 URANS-IBMSG prediction. At $V_{wind} = 24kts$ there was a steady separation at the AIP for both URANS-TRF and URANS-IBMSG and the pre-shock M_{ise} fluctuations reduced to ± 0.02 (Fig. 16).

The comparison of total pressure distribution at the AIP between the unsteady IBMSG and time resolved fan computations also showed that the total pressure losses were mainly generated on the intake lower quadrant and attributed to the ground vortex (Fig. 10). On the lower intake quadrant the level of isentropic Mach number fluctuations on both intake diffuser and lip were slightly different between the URANS-IBMSG and URANS-TRF (Fig. 17). The peak M_{ise} fluctuations were under-predicted by the URANS-IBMSG relative to URANS-TRF at the unsteady separation conditions (Fig. 16). Overall, this highlights an unsteady mechanism of the interaction between the fan and the intake flow field that has an adverse impact on the intake critical operating condition and potentially on the intake design decisions. The next section investigates the mechanisms related to the differences between the two configurations (URANS-IBMSG and URANS-TRF).

3.2.1. Evaluation of the spectrum at post-critical conditions

At $V_{wind} = 30kts$ there was unsteady shock induced separation on the windward side of the intake lip for both URANS-IBMSG and URANS-TRF (Fig. 8). The separation reached the fan face and it extended radially up to about 5% of the fan radius within the intake diffuser (Fig. 18). Although at some instant in time the spatial distribution of the separated flow region looked similar for both URANS-IBMSG and URANS-TRF, the unsteady characteristics of the separated flow region were notably different between URANS-IBMSG and full unsteady simulations (URANS-TRF). The levels of

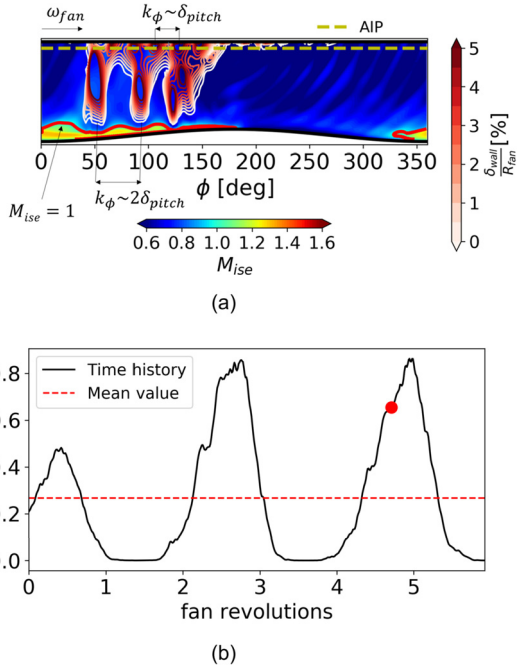

Fig. 18. (a) Time snapshot of unwrapped intake surface with isentropic Mach distribution and isosurface of zero axial velocity; (b) time history of $\dot{m}^-$[%] at AIP. Powered (URANS-TRF) intake configuration at $V_{wind} = 30kts$. Red dot in (b) equates to the instant in time where the flow within the intake is shown in (a).

$\dot{m}^-$[%] fluctuations around the time average value for URANS-IBMSG was notably lower compared to URANS-TRF (Fig. 8). When fan unsteadiness was taken into account (URANS-TRF) the flow at the AIP showed a quasi-periodic oscillation between an attached and a separated condition (Fig. 18). This type of unsteady characteristic was previously reported for more conventional L_{in}/D_{fan} intakes [20,19]. The instantaneous intake flow separation and intake wall M_{ise} distribution for the URANS-TRF were modulated in the azimuthal direction by the blade passing (Fig. 18). Two characteristics azimuthal wavelength (k_ϕ) multiple of the blade pitch angle (δ_{pitch}) can be distinguished. It was found that k_ϕ grows from δ_{pitch} closer to the fan up to $\approx 2\delta_{pitch}$ on the intake lip. This indicates that the azimuthal variation of the static pressure field within the intake due to the fan unsteadiness (URANS-TRF) may notably affect the dynamics of the short intake flow field under crosswind.

At $V_{wind} = 30kts$ the time average M_{ise} axial distribution at $\phi = 90°$ for URANS-IBMSG and URANS-TRF were slightly different with a pre-shock M_{ise} of about $M_{ise} = 1.3$ and 1.32 respectively (Fig. 19). However, URANS-IBMSG substantially under-predicted the peak M_{ise} fluctuations compared with URANS-TRF. The maximum pre-shock isentropic Mach number for the URANS-IBMSG was $M_{ise} = 1.47$ as compared to $M_{ise} = 1.72$ for the URANS-TRF (Fig. 19a). The streamwise velocity fluctuations closer to the fan at $\phi = 90°$ were notably different for URANS-IBMSG and URANS-TRF and in particular the maximum radial extent of the separation was substantially under-predicted by the URANS-IBMSG relative to URANS-TRF (Fig. 19b).

The amplitude of the static pressure fluctuations (P') was normalised with a reference static pressure that corresponded to an ideal value of the static pressure at the nominal fan face (P_{ref}) if an isentropic process within the intake were assumed. Banded spectra of the static pressure fluctuations on a meridional cut through the intake at $\phi = 90°$ identified a spectral signature for both URANS-IBMSG and URANS-TRF within the same frequency band ($f/f_{bp} = \in [0.01, 0.21]$, Fig. 20). The low frequency was associated to an axial displacement of the shock location on the intake

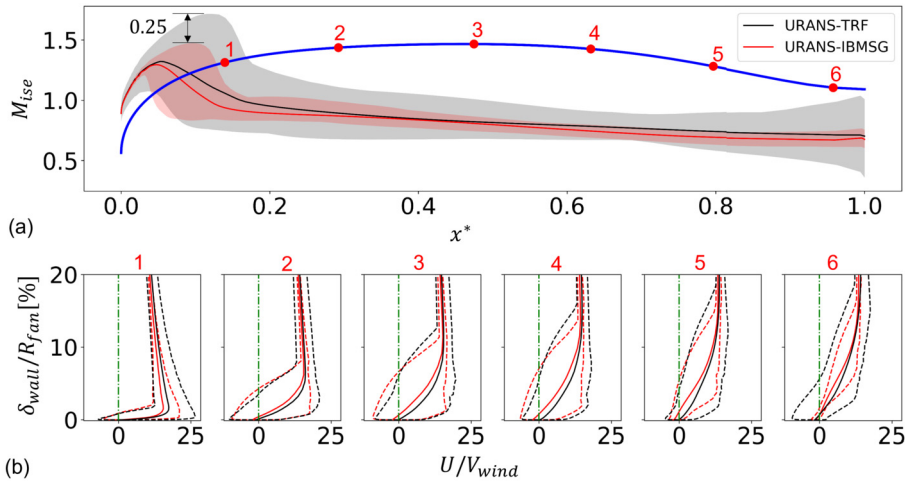

Fig. 19. (a) Isentropic Mach number profiles at $\phi = 90°$; solid line is the time average solution, the shaded region marks the max and minimum values. (b) Streamwise velocity profiles at $\phi = 90°$; solid line is the time average solution, the dashed lines mark the maximum and minimum values. Unsteady powered (URANS-IBMSG and URANS-TRF) configurations at $V_{wind} = 30kts$.

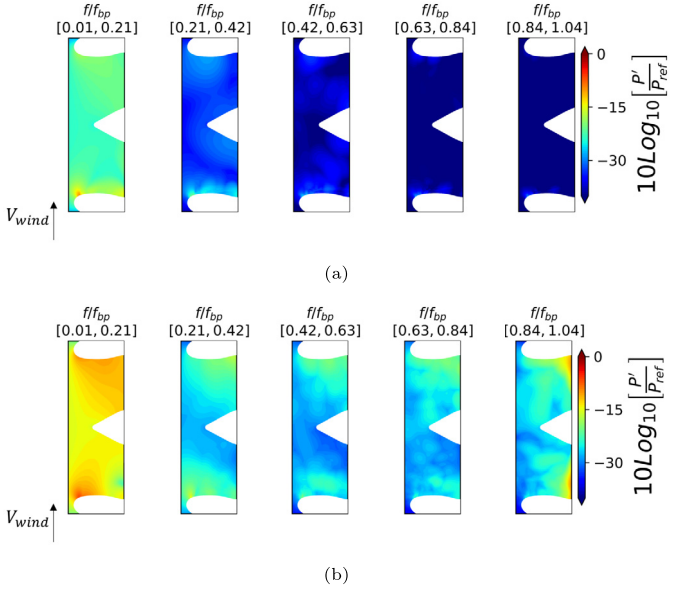

Fig. 20. Banded Fourier spectra of static pressure fluctuations on a meridional plane at $\phi = 90°$. (a) URANS-IBMSG and (b) URANS-TRF at $V_{wind} = 30kts$.

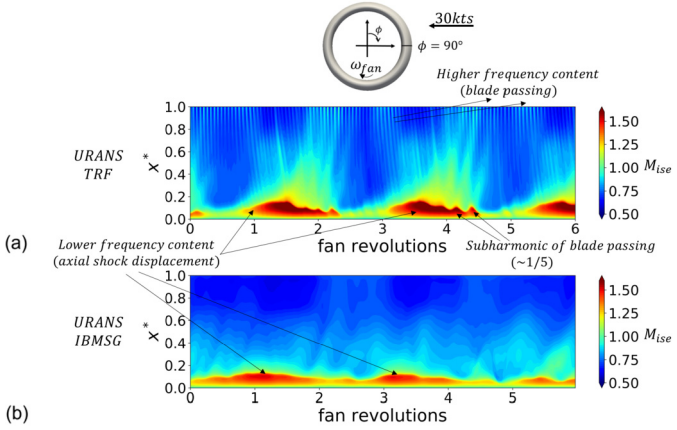

Fig. 21. Temporal variation of intake wall isentropic Mach number distribution at $\phi = 90°$. (a) URANS-TRF and (b) URANS-IBMSG at $V_{wind} = 30kts$.

lip (Fig. 21). For the URANS-TRF the amplitude of the static pressure fluctuations was greater and with a notable signature at blade passing frequency ($f/f_{bp} \in [0.84, 1.04]$, Fig. 20). Moreover, the pulsation of the axial movement of the shock-wave for the URANS-TRF (Fig. 21) was modulated in time at what may be sub-harmonics of the blade passing ($\approx 5t_{bp}$). Overall, fan unsteadiness augmented the post-throat intake separation at the post-critical conditions.

3.2.2. Unsteady flow field at critical conditions

At $V_{wind} = 24kts$ there was steady separation of the intake boundary layer at the AIP for both URANS-IBMSG and URANS-TRF (Fig. 8). At $V_{wind} = 24kts$ within the banded Fourier spectra of the static pressure fluctuations on the intake surface there was a low frequency signature ($f/f_{bp} \in [0.01, 0.21]$) associated to the shock breathing on the windward side of the intake for both URANS-IBMSG and URANS-TRF (Fig. 22). However, the main spectral signature for the URANS-TRF was clearly at blade passing frequency ($f/f_{bp} \in [0.84, 1.04]$). This spectral gap between the main low frequency of the unsteady flow field within the intake and the blade-passing frequency was observed in previous computational work for a short intake at high incidence [16] where a shock pulsation associated with a $f/f_{bp} \approx 0.078$ was reported. The static pressure fluctuations associated with the fan tip pulsation for URANS-TRF ($f/f_{bp} \in [0.84, 1.04]$) propagated up to the shock front on the intake lip although with an expected exponential decay [45] in the amplitude of about 1-2 order of magnitude compared to the value at the nominal fan face (Fig. 22b). The notable contribution of fan unsteadiness on the overall frequency content at $V_{wind} = 24kts$ may be the main reason why, with a further increase in pre-shock Mach number due to an increase of V_{wind}, an unsteady shock wave boundary layer interaction was triggered and the amplitude of the fluctuations on the pre-shock M_{ise} increased (Fig. 16).

The amplitude of the upstream travelling static pressure pulses slightly increased in the ascending blade side of the intake ($\phi \in [180, 360]°$) as the fan exits the distorted flow region (Fig. 22b). It is known that velocity distortions induced by large flow angularity such as those caused by the presence of a ground vortex can notably reduce the fan stall margin [28]. Thus, it is important to evaluate the impact of flow inhomogeneities at the AIP from the fan perspective. At $V_{wind} = 24kts$ there was a notable variation of the time average distribution of blade incidence angle ($i = \beta - \beta_{ma}$) at the AIP on the lower intake quadrant where the ground vortex was ingested (Fig. 23). The ground vortex was counter-rotating compared to the fan and an increase in blade incidence angle towards the tip was expected due to the counter-rotating swirl in-

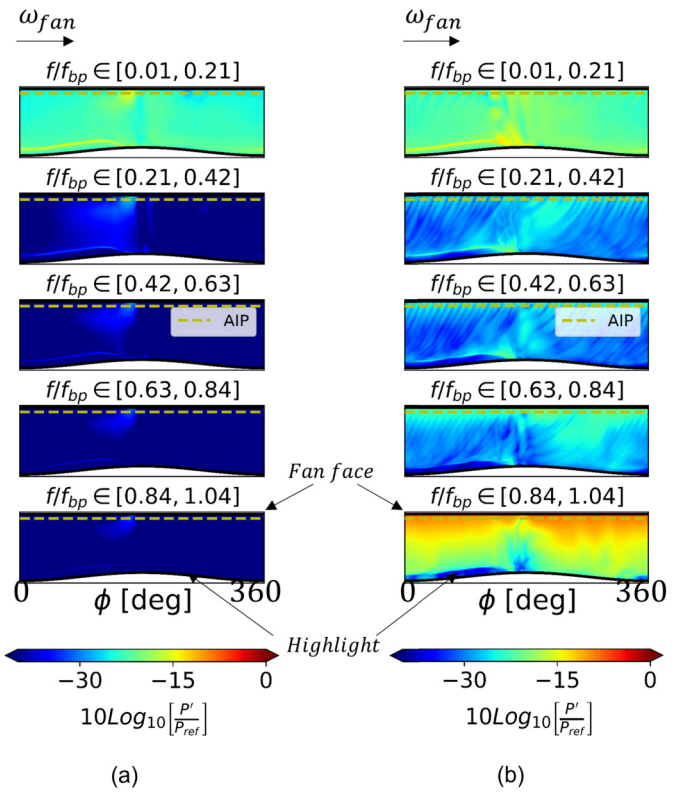

Fig. 22. Banded Fourier spectra of static pressure fluctuations on the intake surface. (a) URANS-IBMSG and (b) URANS-TRF at $V_{wind} = 24kts$.

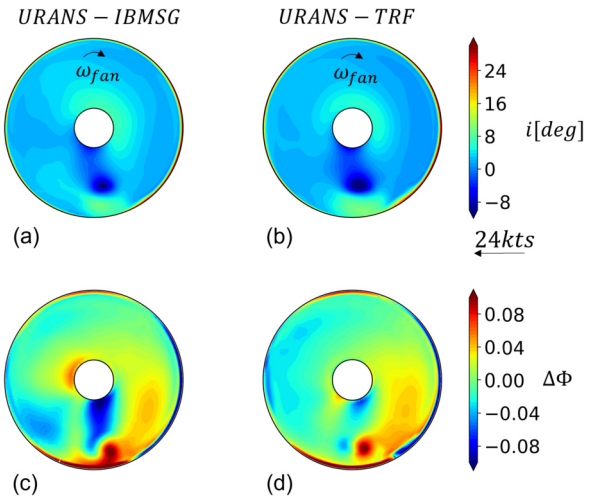

Fig. 23. (a), (b) Time average blade incidence angle (i) and (c), (d) time average flow coefficient deviation ($\Delta\Phi$) distributions at the AIP at $V_{wind} = 24kts$.

duced by the ground vortex itself. However, the ground vortex also induced a co-swirl at about 70% of the fan radius which caused a negative i up to $i \approx -10°$ and a notable spanwise variation of the blade incidence angle at $\phi \approx 180°$ (Fig. 23a, b). A flow coefficient deviation [16] was defined as

$$\Delta\Phi = \Phi(r, \theta) - \Phi_{avg}(r) \tag{8}$$

where $\Phi = V_x/(\omega_{fan} r)$ and Φ_{avg} is the circumferentially averaged flow coefficient at a certain radial position. At $V_{wind} = 24kts$ the ground vortex introduced a notable variation in the flow coefficient on the lower intake quadrant ($\phi \approx 180°$) with an overall increase in $\Delta\Phi$ towards the tip section (Fig. 23c, d). Thus, the ground vortex may further increased the blade loading towards the tip section which contributed to a consequent increase in the amplitude of the fan tip pulsation and the static pressure fluctuations on the ascending blade side of the intake wall (Fig. 22b at $f/f_{bp} \in [0.84, 1.04]$).

3.2.3. Interaction between fan unsteadiness and SBLI

The previous section showed that for the URANS-TRF simulations at the critical condition ($V_{wind} = 24kts$) the amplitude of the static pressure fluctuations at blade passing frequency represented a notable contribution within the overall frequency content (Fig. 22b). Thus, the instantaneous amplitude of the pulsations from the fan tip that reached the intake throat at $V_{wind} = 24kts$ needs to be quantified in terms of the fluctuations introduced in the azimuthal distribution of absolute Mach number at blade-passing EO. At a radial position (r) of about 95% of the intake throat radius ($r_{th,\phi=90°}$) the peak-to-peak amplitude in the azimuthal distribution of the absolute Mach number (ΔM_{p2p}) was $\Delta M_{p2p} \approx 0.055$ (Fig. 24). The amplitude of these periodic acoustic disturbances associated with fan tip pulsation may be strong enough to impose a difference in the static pressure ratio across the shock which will in turn change its axial location to modulate its relative strength and match the new imposed pressure ratio [46,47].

Thus, it was overall argued that the intake flow unsteadiness predicted by URANS-TRF for $V_{wind} \geq 26kts$ was triggered by the fan unsteadiness which in turn leads to about $4kts$ ($\approx 15\%$) penalty in the prediction of intake critical condition (Fig. 8) relative to the model where fan unsteadiness was not considered (URANS-IBMSG). Overall, it was observed that there are two competing mechanisms involved in fan-intake coupling which may impact the intake critical conditions. The first is the beneficial effect of the radial mass flow redistribution at the AIP due to the fan. This increases the critical crosswind velocity from approximately $V_{wind} = 20kts$ to $V_{wind} = 28kts$. The second is an adverse effect due to fan unsteadiness which reduces the critical crosswind velocity from $V_{wind} = 28kts$ to $V_{wind} = 24kts$.

4. Conclusions

This work explored a hierarchy of numerical fan models for fan-intake coupled analyses in crosswind. Two competing mechanisms were identified and both were important to establish the impact of the fan on a short intake in crosswind conditions. Mass flux redistribution due to the fan had a notable beneficial impact on the reduction of total pressure loss at the AIP at post-separation condition compared to an aspirated configuration. This is similar to previously reported benefits of the fan interaction under high incidence conditions. However, the fan unsteadiness on a short intake in crosswind can induce a modulation on the intake flow which augments the post-throat intake separation. Moreover, the periodic azimuthal changes in the static pressure field due to the rotating fan blades triggered an unsteady shock-wave boundary layer interaction. The unsteady interaction due to the fan unsteadiness results in an adverse 15% reduction in the critical velocity for the intake operating in crosswind conditions. Thus, the impact of the fan on the separation onset and characteristics of the boundary layer within a short intake in crosswind is composed by both steady and unsteady terms that for the present case study had a different polarity and represented a benefit and a penalty respectively. The present work overall proposed a characterisation of the mechanisms involved in fan-intake coupling which affect the prediction of intake critical conditions and the preliminary choices for short intake design.

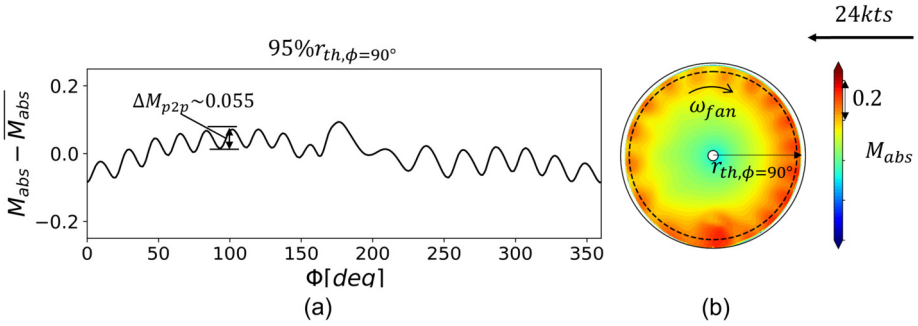

Fig. 24. (a) Azimuthal variation of absolute Mach number (M_{abs}) and (b) M_{abs} distribution at the intake throat. Time snapshots for the powered (URANS-TRF) configuration at $V_{wind} = 24kts$.

Declaration of competing interest

The authors declare that they have no known competing financial interests or personal relationships that could have appeared to influence the work reported in this paper.

Data availability

All data underlying the results are available as part of the article and no additional source data are required.

Acknowledgements

The doctoral studies of Luca Boscagli were partially funded by Rolls-Royce, plc., and the Engineering and Physical Sciences Research Council industrial case award 16000032.

References

[1] F. Tejero, M. Robinson, D.G. MacManus, C. Sheaf, Multi-objective optimisation of short nacelles for high bypass ratio engines, Aerosp. Sci. Technol. 91 (2019) 410–421, https://doi.org/10.1016/j.ast.2019.02.014.
[2] J.J. Otter, T. Stańkowski, M. Robinson, D.G. MacManus, Installation aerodynamics of civil aero-engine exhaust systems, Aerosp. Sci. Technol. 89 (2019) 345–355, https://doi.org/10.1016/j.ast.2019.03.046.
[3] M. Robinson, D.G. MacManus, R. Christie, C. Sheaf, N. Grech, Nacelle design for ultra-high bypass ratio engines with CFD based optimisation, Aerosp. Sci. Technol. 113 (2021) 106191, https://doi.org/10.1016/j.ast.2020.106191.
[4] I. Goulos, J. Otter, F. Tejero, J. Hueso Rebassa, D. MacManus, C. Sheaf, Civil turbofan propulsion aerodynamics: thrust-drag accounting and impact of engine installation position, Aerosp. Sci. Technol. 111 (2021) 106533, https://doi.org/10.1016/j.ast.2021.106533.
[5] A. Coschignano, H. Babinsky, C. Sheaf, E. Platt, Influence of near-leading edge curvature on the performance of aero-engine intake lips at high-incidence, in: 34th AIAA Applied Aerodynamics Conference, (June) 2016.
[6] A. Coschignano, N. Atkins, H. Babinsky, J. Serna, Effect of Reynolds number on a normal shock wave-transitional boundary-layer interaction over a curved surface, Exp. Fluids 60 (12) (2019) 1–12, https://doi.org/10.1007/s00348-019-2824-0.
[7] A. Peters, Z.S. Spakovszky, W.K. Lord, B. Rose, Ultrashort nacelles for low fan pressure ratio propulsors, J. Turbomach. 137 (2) (2015), https://doi.org/10.1115/1.4028235.
[8] T. Cao, N.R. Vadlamani, P.G. Tucker, A.R. Smith, M. Slaby, C.T. Sheaf, Fan-intake interaction under high incidence, J. Eng. Gas Turbines Power 139 (4) (2017) 1–10, https://doi.org/10.1115/1.4034701.
[9] Y. Ma, N.R. Vadlamani, J. Cui, P. Tucker, Comparative studies of RANS versus large Eddy simulation for fan-intake interaction, J. Fluids Eng., Trans. ASME 141 (3) (2019) 1–13, https://doi.org/10.1115/1.4041393.
[10] T. Cao, P. Hield, P.G. Tucker, Hierarchical immersed boundary method with smeared geometry, J. Propuls. Power 33 (5) (2017) 1151–1163, https://doi.org/10.2514/1.B36190.
[11] Y. Ma, J. Cui, N.R. Vadlamani, P. Tucker, Effect of fan on inlet distortion: mixed-fidelity approach, AIAA J. 56 (6) (2018) 2350–2360, https://doi.org/10.2514/1.J056858.
[12] M. Carnevale, F. Wang, L.D. Mare, Low frequency distortion in civil aero-engine intake, J. Eng. Gas Turbines Power 139 (4) (2017), https://doi.org/10.1115/1.4034600.
[13] W. Zhang, M. Vahdati, A parametric study of the effects of inlet distortion on fan aerodynamic stability, J. Turbomach. 141 (1) (2019), https://doi.org/10.1115/1.4041376.
[14] A.J. Provenza, K.P. Duffy, M.A. Bakhle, Aeromechanical response of a distortion-tolerant boundary layer ingesting fan, J. Eng. Gas Turbines Power 141 (1) (jan 2019), https://doi.org/10.1115/1.4040739.
[15] E.J. Gunn, S.E. Tooze, C.A. Hall, Y. Colin, An experimental study of loss sources in a fan operating with continuous inlet stagnation pressure distortion, J. Turbomach. 135 (3) (2013), https://doi.org/10.1115/1.4007835.
[16] N.R. Vadlamani, T. Cao, R. Watson, P.G. Tucker, Toward future installations: mutual interactions of short intakes with modern high bypass fans, J. Turbomach. 141 (8) (2019) 1–11, https://doi.org/10.1115/1.4044080.
[17] B. Mohankumar, C.A. Hall, M.J. Wilson, Fan aerodynamics with a short intake at high angle of attack, in: Proceedings of the ASME Turbo Expo 2A-2020, 2020, pp. 1–13, https://doi.org/10.1115/GT2020-16296.
[18] J. Murphy, Intake Ground Vortex Aerodynamics, Phd thesis, Cranfield University, 2008, http://hdl.handle.net/1826/3515.
[19] C. Freeman, A.L. Rowe, Intake Engine Interactions of a Modern Large Turbofan Engine, vol. 1, 1999, https://doi.org/10.1115/99-GT-344.
[20] C.A. Hall, T.P. Hynes, Nacelle interaction with natural wind prior to take-off, in: 38th AIAA/ASME/SAE/ASEE Joint Propulsion Conference and Exhibit, July 2002, pp. 1–11, https://doi.org/10.2514/6.2002-3773.
[21] C.A. Hall, T.P. Hynes, Measurements of Intake Separation Hysteresis in a Model Fan and Nacelle RIG, 38th AIAA/ASME/SAE/ASEE Joint Propulsion Conference and Exhibit, vol. 22(4), 2002, https://doi.org/10.2514/6.2002-3772.
[22] Y. Colin, B. Aupoix, J. Boussuge, P. Chanez, Numerical Simulation of the Distortion Generated by Crosswind Inlet Flows, Isabe-2007-1210, 2007, pp. 1–13.
[23] N.R. Vadlamani, P.G. Tucker, Eddy Resolving Simulations of Intake Under Crosswinds, vol. 25, Springer International Publishing, 2019, https://doi.org/10.1007/978-3-030-04915-7_69.
[24] M. Burnazzi, A. Probst, M. Steger, Hybrid RANS/LES of an isolated engine nacelle with crosswind using an unstructured CFD solver, in: Progress in Hybrid RANS-LES Modelling, Springer, 2020, pp. 347–356.
[25] R. Schnell, D. Schönweitz, M. Theune, J. Corroyer, Integration- and intake-induced flow distortions and their impact on aerodynamic fan performance, in: Symposium on Field of the Research Unit 1066, Springer, 2014, pp. 251–269.
[26] Q.J. Minaker, J.J. Defoe, Prediction of crosswind separation velocity for fan and nacelle systems using body force models: part 1: Fan body force model generation without detailed stage geometry, Int. J. Turbomach., Prop. Power 4 (4) (2019), https://doi.org/10.3390/ijtpp4040043.
[27] K.-B. Lee, M. Wilson, M. Vahdati, Effects of inlet disturbances on fan stability, J. Eng. Gas Turbines Power 141 (5) (may 2019), https://doi.org/10.1115/1.4042204.
[28] A. Awes, A. Brosse, G. Dufour, X. Carbonneau, B. Godard, Effect of a vortex distortion on the operability of an ultra high bypass ratio fan, in: Proceedings of the ASME Turbo Expo 2A-2020, 2020, pp. 1–11, https://doi.org/10.1115/GT2020-14596.
[29] P. Moinier, Algorithm developments for an unstructured viscous flow solver, Phd thesis, Oxford University, 1999.
[30] P.I. Crumpton, P. Moinier, M.B. Giles, An unstructured algorithm for high Reynolds number flows on highly stretched grids, in: Proceedings of the 10th International Conference on Numerical Methods for Laminar and Turbulent Flows, 1997, pp. 21–25.
[31] C. Misev, N.J. Hills, Steepest descent optimisation of Runge–Kutta coefficients for second order implicit finite volume CFD codes, J. Comput. Phys. 354 (2018) 576–592, https://doi.org/10.1016/j.jcp.2017.09.008.
[32] G. Almendral-Fernandez, D. Amirante, N.J. Hills, Use of a zonal hybrid URANS-LES methodology for prediction of rim seal ingestion into a low pressure turbine cavity, in: 2018 Joint Propulsion Conference, 2018, https://doi.org/10.2514/6.2018-4917.
[33] P.R. Spalart, S.R. Allmaras, One-equation turbulence model for aerodynamic flows, Rech. Aérosp. 1 (1994) 5–21, https://doi.org/10.2514/6.1992-439.

[34] J.D. Denton, The Calculation of Three-Dimensional Viscous Flow Through Multistage Turbomachines, Journal of Turbomachinery 114 (1) (1992) 18–26, https://doi.org/10.1115/1.2927983, https://asmedigitalcollection.asme.org/turbomachinery/article-pdf/114/1/18/5604229/18_1.pdf.
[35] J. Seddon, E.L. Goldsmith, Intake Aerodynamics, vol. 2, Blackwell Science, Oxford, 1999.
[36] I.B. Celik, U. Ghia, P.J. Roache, C.J. Freitas, H. Coleman, P.E. Raad, Procedure for estimation and reporting of uncertainty due to discretization in CFD applications, J. Fluids Eng., Trans. ASME 130 (7) (2008) 0780011, https://doi.org/10.1115/1.2960953.
[37] I. CFD, ANSYS ICEM CFD User's Manual, 2016.
[38] A. Milli, S. Shahpar, Padram: parametric design and rapid meshing system for complex turbomachinery configurations, in: Proceedings of the ASME Turbo Expo 8 (Parts A, B, and C), 2012, pp. 2135–2148.
[39] J.P. Murphy, D.G. MacManus, Ground vortex aerodynamics under crosswind conditions, Exp. Fluids 50 (1) (2011) 109–124, https://doi.org/10.1007/s00348-010-0902-4.
[40] S. Zantopp, D. MacManus, J. Murphy, Computational and experimental study of intake ground vortices, Aeronaut. J. 114 (1162) (2010) 769–784, https://doi.org/10.1017/S0001924000004255.
[41] A. Coschignano, H. Babinsky, Boundary-layer development downstream of normal shock in transonic intakes at incidence, AIAA J. 57 (12) (2019) 5241–5251, https://doi.org/10.2514/1.j058508.
[42] Z. Wang, I. Gursul, Unsteady characteristics of inlet vortices, Exp. Fluids 53 (4) (2012) 1015–1032, https://doi.org/10.1007/s00348-012-1340-2.
[43] J.W. Cooley, J.W. Tukey, An algorithm for the machine calculation of complex Fourier series, Math. Comput. 19 (90) (1965) 297–301.
[44] B.G. Van Der Wall, H. Richard, Analysis methodology for 3C PIV data, in: 31st European Rotorcraft Forum 2005, 2005.
[45] J.M. Tyler, T.G. Sofrin, Axial flow compressor noise studies, SAE Technical Papers, https://doi.org/10.4271/620532, 1962.
[46] P.J. Bruce, H. Babinsky, Unsteady shock wave dynamics, J. Fluid Mech. 603 (2008) 463–473, https://doi.org/10.1017/S0022112008001195.
[47] P.J. Bruce, H. Babinsky, An experimental study of transonic shock/boundary layer interactions subject to downstream pressure perturbations, Aerosp. Sci. Technol. 14 (2) (2010) 134–142, https://doi.org/10.1016/j.ast.2009.11.006.